Supporting Information for: Impact of the Dynamic Electron Correlation on the Unusually Long Excited State Lifetime of Thymine

Woojin Park,[†] Seunghoon Lee,[*,‡] Miquel Huix-Rotllant,[*,¶] Michael Filatov,[*,†] and Cheol Ho Choi[*,†]

†*Department of Chemistry, Kyungpook National University, Daegu 41566, South Korea*

‡*Division of Chemistry and Chemical Engineering, California Institute of Technology, Pasadena, California 91125, USA*

¶*Aix-Marseille Univ, CNRS, ICR, Marseille 13397, France*

E-mail: slee89@caltech.edu; miquel.huixrotllant@univ-amu.fr; mike.filatov@gmail.com; cchoi@knu.ac.kr

List of Figures

List of Tables

Methodology and Computational Details

MRSF not only alleviates the problem of spin-contamination of SF-TDDFT[3] but also removes the problematic identification process of spin state.[4] In addition, an important advantage of MRSF before the usual linear-response TDDFT[5–7] is that MRSF enables proper computation of the S_1/S_0 conical intersections (since both states belong to the same response states in MRSF);[8] which is crucial for the accurate description of the dynamics of the excited states. Additionally, MRSF not only includes singly but also some important doubly excited configurations in its approximate wavefunctions. The latter is completely missing in the LR-TDDFT, limiting its descriptions of excited states.

Detailed discussion of MRSF-TDDFT can be found else where.[9,10] The main concept is summarized in this section. Derivation of the MRSF-TDDFT methodology[9] is based on the density-matrix formulation of time-dependent Kohn-Sham theory.[11] In MRSF-TDDFT, the zeroth-order mixed-reference reduced density matrix (MR-RDM), $\rho_0^{\mathrm{MR}}(x, x')$, is defined by satisfying an idempotence relation,

$$\rho_0^{\mathrm{MR}}(x, x') = \int \rho_0^{\mathrm{MR}}(x, x'')\rho_0^{\mathrm{MR}}(x'', x')dx'', \tag{S1}$$

and its density, $\rho_0^{\mathrm{MR}}(x) = \rho_0^{\mathrm{MR}}(x, x)$, is same as an equiensemble density of M_S = +1 and $M_S = -1$ components of a triplet state, *e.g.*,

$$\rho_0^{\mathrm{MR}}(x) = \frac{1}{2}\left\{\rho_0^{M_S=+1}(x) + \rho_0^{M_S=-1}(x)\right\}. \tag{S2}$$

Within the Tamm-Dancoff approximation,[12,13] the use of MR-RDM in the linear-response formalism yields completely decoupled two linear-response equations for singlet and triplet excited states, respectively,[9]

$$\sum_{rs}\left(A^{(k)(0)}_{pq,rs} + A'^{(k)}_{pq,rs}\right)X^{(k)}_{rs} = \Omega_{(k)}X^{(k)}_{pq}, \qquad k = S, T \tag{S3}$$

where $k = S, T$ labels singlet and triplet states, $A^{(k)(0)}_{pq,rs}$ is an orbital Hessian matrix derived by the linear response, and $A'^{(k)}_{pq,rs}$ is a coupling matrix between configurations originating from different components, $M_S = +1$ and $M_S = -1$, of the mixed reference.[9,10] $X^{(k)}_{pq}$ and $\Omega_{(k)}$ are the amplitude vectors and the excitation energies with respect to the reference state, respectively. Because the singlet and triplet response states are generated by different response equations, there is no mixing between the two different groups of responses. This is a great advantage of MRSF-TDDFT over SF-TDDFT, since only one group of response states is produced by the latter theory, requiring further identification of spin state of its response states.

It was shown that a linear response of MRSF-TDDFT can be represented as configurations from $M_S = +1$ and $M_S = -1$ references depicted as those with black and red arrows, respectively, in Fig. S1.[9] The configurations with the red arrows are missing in the conventional SF-TDDFT; their absence leads to spin contamination of the response states. These are recovered in MRSF-TDDFT and the spin contamination of the response states is nearly eliminated.[9] Configurations with the blue arrows are originated from both $M_S = +1$ and $M_S = -1$ components of the mixed reference. Although not all electronic configurations can be recovered by using the MR-RDM, the missing C $\rightarrow$ V configurations (depicted with gray arrows in Fig. S1) represent high-lying excited states and their effect on the lower part of the excitation spectrum is insignificant.[9] As the MRSF-TDDFT method is computationally inexpensive, the energy derivatives are easily available[10] and it gives reasonable vertical-excitation energies for organic molecules,[14] this method is very well suited for modeling the dynamics of thymine, which may require running simulations for long times, on the range of several picoseconds. Here, we use the MRSF-TDDFT method to study the multi-state non-adiabatic dynamics of thymine initiated in the optically bright S_2 state and including the S_2, S_1, and S_0 states. To analyze the results of the NAMD TSH simulations the geometries of critical species, the local minima and the conical intersections, were optimized. In addition, the minimum energy paths among

them were generated using the nudged elastic band method.[15,16]

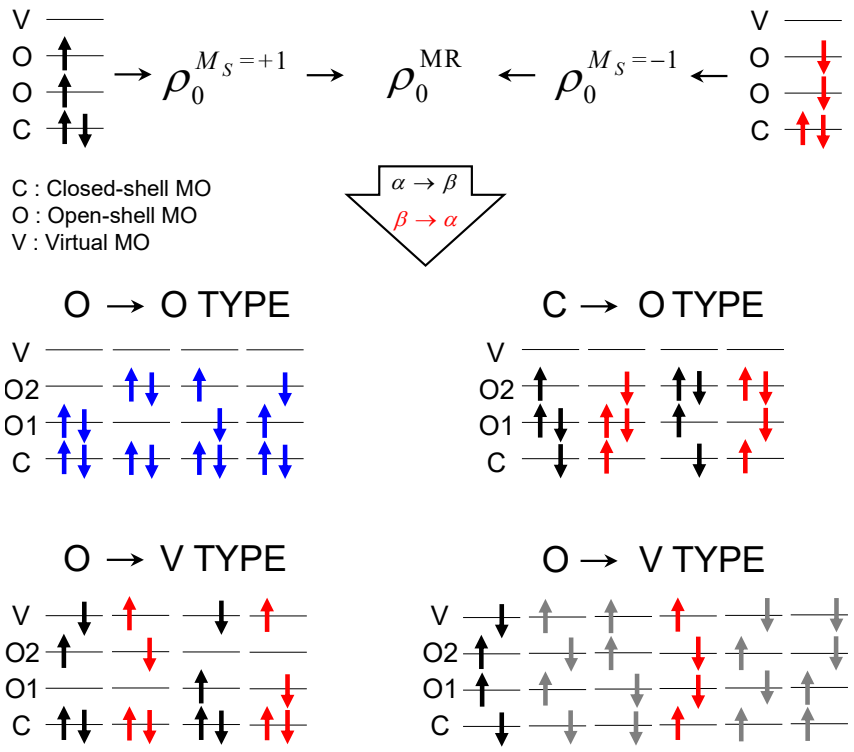

Figure S1: Electronic configurations of the $M_S = +1$ and $M_S = -1$ components of triplet reference in the upper panel and a complete set of configurations for MRSF-TDDFT in the lower panel. Response states are described by configurations represented with blue, black, and red arrows in MRSF-TDDFT, while with blue and black arrows in SF-TDDFT.

Vertical excitation energies of thymine.

At the S_0 equilibrium geometry, the most accurate *ab initio* methods in Table S1, the MR-CISD+Q and EOM-CCSD methods, yield the vertical excitation energies (VEE) to the dark (S_1, $n \rightarrow \pi^*$) and the bright (S_2, $\pi \rightarrow \pi^*$) states at *ca.* 5 eV and 6 eV, respectively. These VEEs are consistent with the experimental measurements based on the electron energy loss spectroscopy (EELS), which yields excitation energies in the range of 4.9 – 4.96 eV and 5.75 – 6.2 eV. Note, however, that the EELS energies may be closer to the adiabatic excitation energies, rather than vertical. Nevertheless, there is a rather good agreement between the VEEs obtained using MRCISD+Q and EOM-CCSD and the MRSF VEEs, see Table S1.

Table S1: Vertical excitation energies of the lowest singlet excited states of thymine in the gas phase with several methods. All energies are relative to the respective ground state minimum energy. Oscillator strength are given in the parentheses. See Fig. S2 for frontier orbitals of thymine.

Method	$S_0(\pi^2) \rightarrow S_1(n\pi^*)$	$S_0(\pi^2) \rightarrow S_2(\pi\pi^*)$
	Vertical Excitations	
MRSF-TD / 6-31G* / BH&HLYP[a)]	5.83 (0.00)	6.00 (0.62)
LR-TDDFT / 6-31G* / BH&HLYP[b)]	5.47 (0.00)	5.77 (0.23)
LR-TDDFT / SVP / PBE0[c)]	4.85	5.44
ADC(2) / aug-cc-pVDZ[d)]	4.56	5.06
CASSCF (8e, 6o) / 6-31G*[e)]	5.31	7.12
MS-CASPT2 (12e, 9o)[e)]	5.09	5.09
MRCISD+Q / 3-21G*[f)]	5.26	6.08
EOM-CCSD[f)] / 6-311G**	5.29	5.80
CC2 / aug-cc-pVTZ[g)]	4.82	5.20
CASPT2 (10e, 14o) / ANO[h)]	4.39 (0.00)	4.88 (0.17)
	Experimentals	
EEL spectroscopy (gas)[i)]	4.95, 6.2, 7.4 (all values $\pm$ 0.08)	
EEL spectroscopy (gas)[j)]	4.9, 6.0, 6.3, 7.3	
EEL spectroscopy (gas)[k)]	4.96, 5.75, 6.17	

[a)] This work. [b)] at MRSF-TD / 6-31G* / BH&HLYP optimized geometry. [c)] from Ref. 17
[d)] from Ref. 18 aug-cc-pVDZ for all elements except for hydrogen, where cc-pVDZ was employed.
[e)] from Ref. 19. MS-CASPT2 has been carried out using a CASSCF(12,9)/6-311G* reference function.
[f)] from Ref. 20. [g)] from Ref. 21. [h)] from Ref. 22. [i)] from Ref. 23. [j)] from Ref. 24. [k)] from Ref. 25.

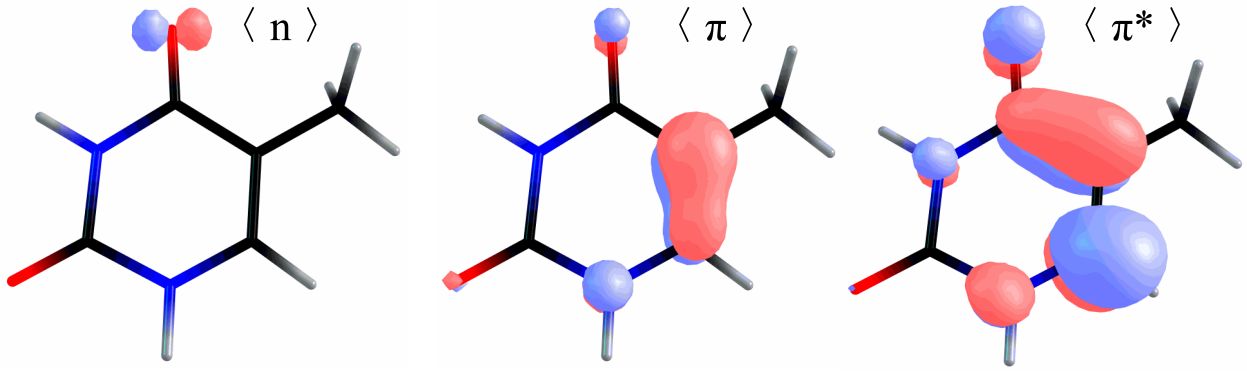

Figure S2: Frontier orbitals of thymine.

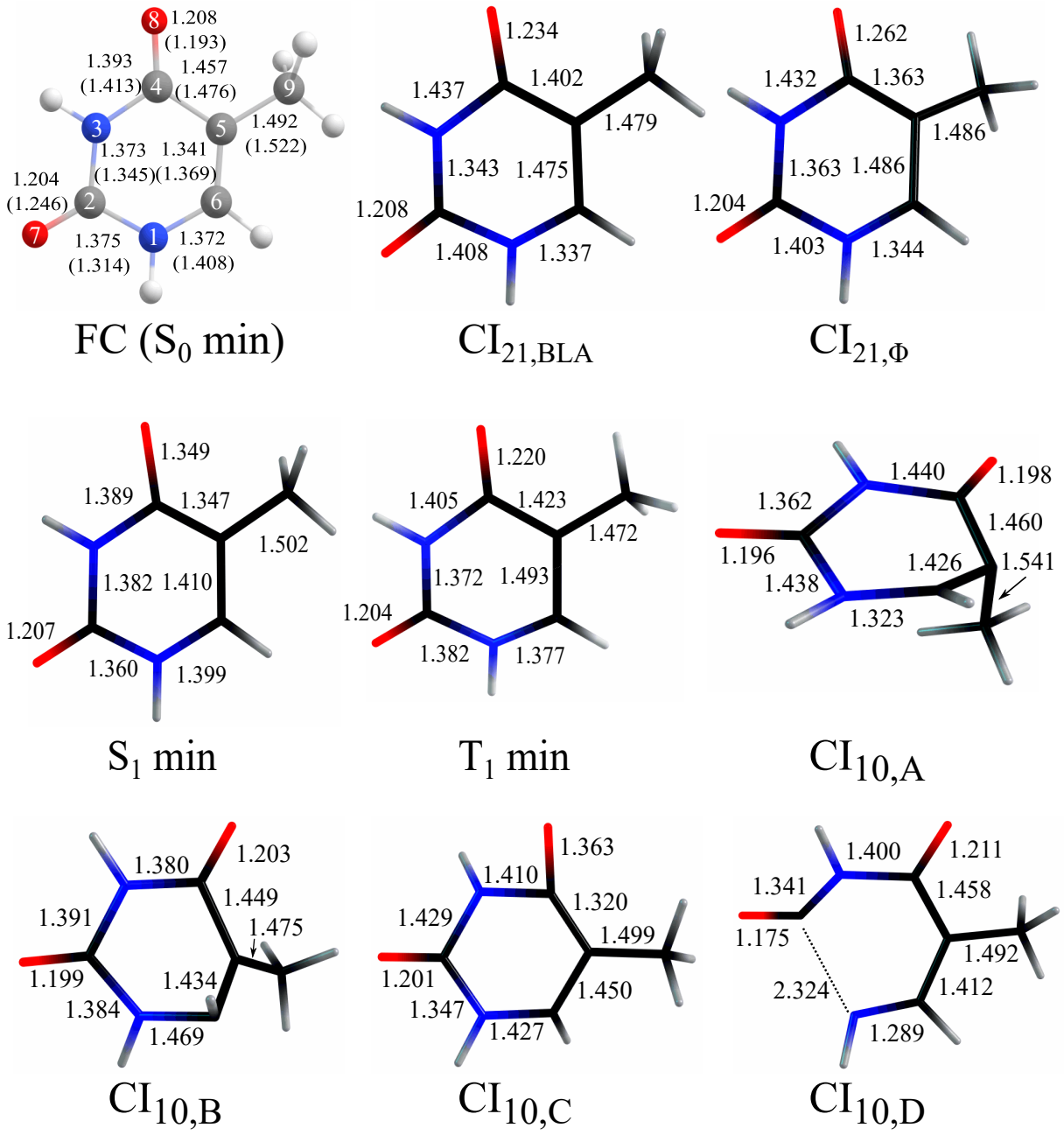

Figure S3: Optimized geometry of ground state with atom numbering and crystallographic data[1] given in parenthesis, $CI_{21,BLA}$, $CI_{21,\phi}$, S_1 minimum, T_1 minimum, $CI_{10,A}$, $CI_{10,B}$, $CI_{10,C}$, and $CI_{10,D}$ with bond length in Å. Geometries of FC, $CI_{21,BLA}$, and S_1 minimum feature flat pyrimidine ring. The (ΔE/eV, BLA/Å, ϕ/°) values are; FC (6.00, 0.000, 0.03) (S_2 energy), $CI_{21,BLA}$ (5.49, 0.135, 0.02), $CI_{21,\phi}$ (5.26, 0.194, 43.9), S_1 minimum (4.33, 0.215, -0.02), T_1 minimum (3.41, 0.122, 27.12), $CI_{10,A}$ (4.58, 0.035, 115.3), $CI_{10,B}$ (5.33, 0.0020, 72.9), $CI_{10,C}$ (5.86, 0.269, -31.1), $CI_{10,D}$ (4.83, 0.036, 6.64).

Stationary points, and Minimum Energy Potential Surfaces

The ground state equilibrium geometry (FC), $CI_{21,BLA}$, $CI_{21,\phi}$, S_1 minimum, T_1 minimum, and four CIs between S_1 and S_0 of thymine optimized with the MRSF-TD-BH&HLYP/6-31G* method in the gas phase are shown in the of Fig. S3, where it is compared with the experimental geometry from the crystallographic data[1] given parenthetically. The S_0 equilibrium geometry of thymine obtained with MRSF/BH&HLYP/6-31G* method is in excellent agreement with the experimental crystallographic geometry; see Fig. S3. The optimized S_0 equilibrium geometry features flat pyrimidine ring and the optimized bond lengths are in a good agreement with the crystallographic data; the average deviation of the bond lengths is 0.031 Å. As the consequence of populating the π^* orbital, the C_5=C_6 π-bond is partially broken and this leads to lengthening of the C_5=C_6. The neighboring C_4–C_5 bond and C_4=O_8 are simultaneously shortened and lengthened as the π^* orbital has bonding and anti-bonding characteristic between these atoms respectively; see Fig. S2 for frontier orbitals of thymine. $CI_{21,BLA}$ and S_1 minimum have flat ring with a substantial BLA along the π-conjugation. $CI_{21,\phi}$, which is considered as a conventional decay channel from S_2 to S_1, has not only BLA of the chain, but also ring puckering at the C_6 atom; See Fig. S3 for atom numbering. Three CIs($CI_{10,A}$, $CI_{10,B}$, and $CI_{10,C}$) feature out of plane displacement of the methyl group. The ϕ value of $CI_{10,A}$ and $CI_{10,B}$ are positive(115.3, 72.9 respectively) and that of $CI_{10,C}$ is negative (-31.14). This indicates that $CI_{10,A}$, $CI_{10,B}$ have torsion of methyl group in the same direction, whereas $CI_{10,C}$ has opposite direction. In addition, we locate new $CI_{10,D}$ which has substantial elongation on C_4–N_6 without changing torsion. The BLA value of $CI_{21,BLA}$ and S_1 minimum is 0.14 and 0.22 respectively, meaning that $CI_{21,BLA}$ is close to FC geometry while S_1 minimum is relatively far from FC geometry and exhibits an inversion of double bond(C_4=O_8, C_5=C_6) and single point(C_4–C_5); see Fig. S3. According to Zechmann and Barbatti[20] the S_1/S_0 CIs can be classified as follows:

$CI_{10,A}$ (MXS1 in ref. 20) : ${}^1\pi^2/{}^1\pi\pi^*$

$CI_{10,B}$ (MXS2 in ref. 20) : $^1\pi^2/^1\pi\pi^*$

$CI_{10,C}$ (MXS8 ref. 20) : $^1(\pi^2+\pi\pi^*)/^1n\pi^*$

$CI_{10,D}$ (a minor CI) : $^1(\pi^2+\pi n^*)/^1(\pi^2+\pi n^*)$.

Hence, these CIs occur in different regions of the S_1 and S_0 potential energy surfaces, as indicated by their electronic characteristics.

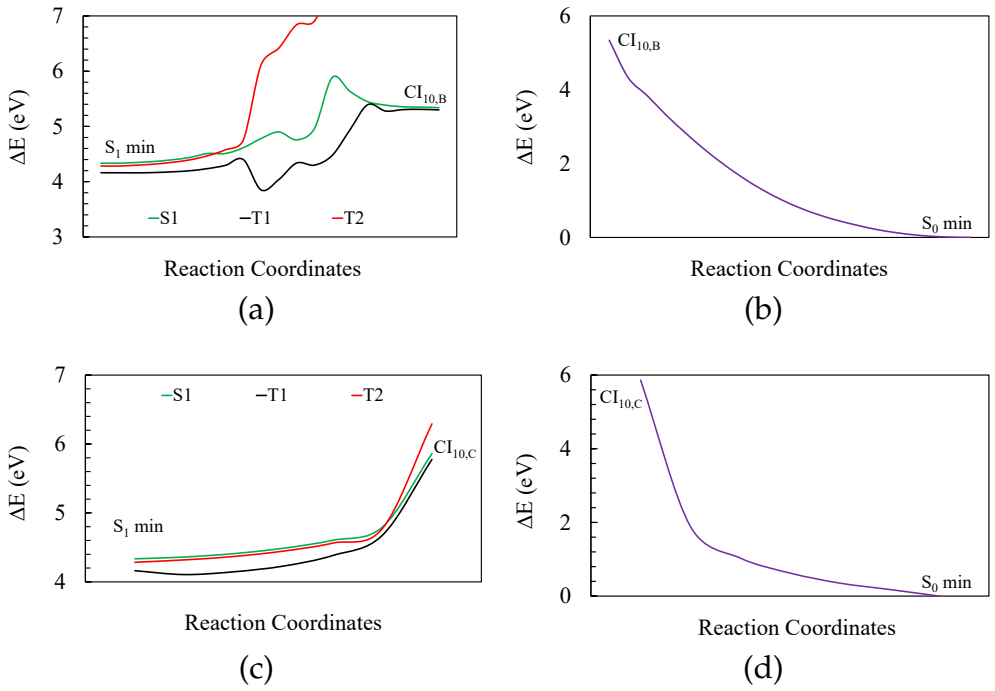

Figure S4: 2D MEPs connecting (a) S_1 min to $CI_{10,B}$, (b) $CI_{10,B}$ to S_0 min, (c) S_1 min to $CI_{10,C}$, and (d) $CI_{10,C}$ to S_0 min.

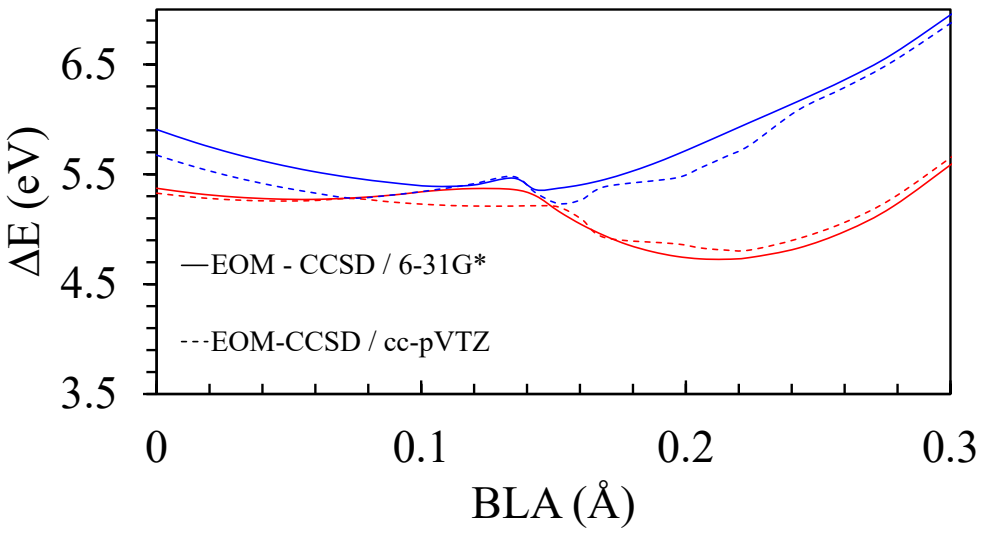

Figure S5: The S_2 (blue) and S_1 (red) MRSF BLA PES profiles along the EOM-CCSD / 6-31G* (solid line), and EOM-CCSD / cc-pVTZ (dashed lines).

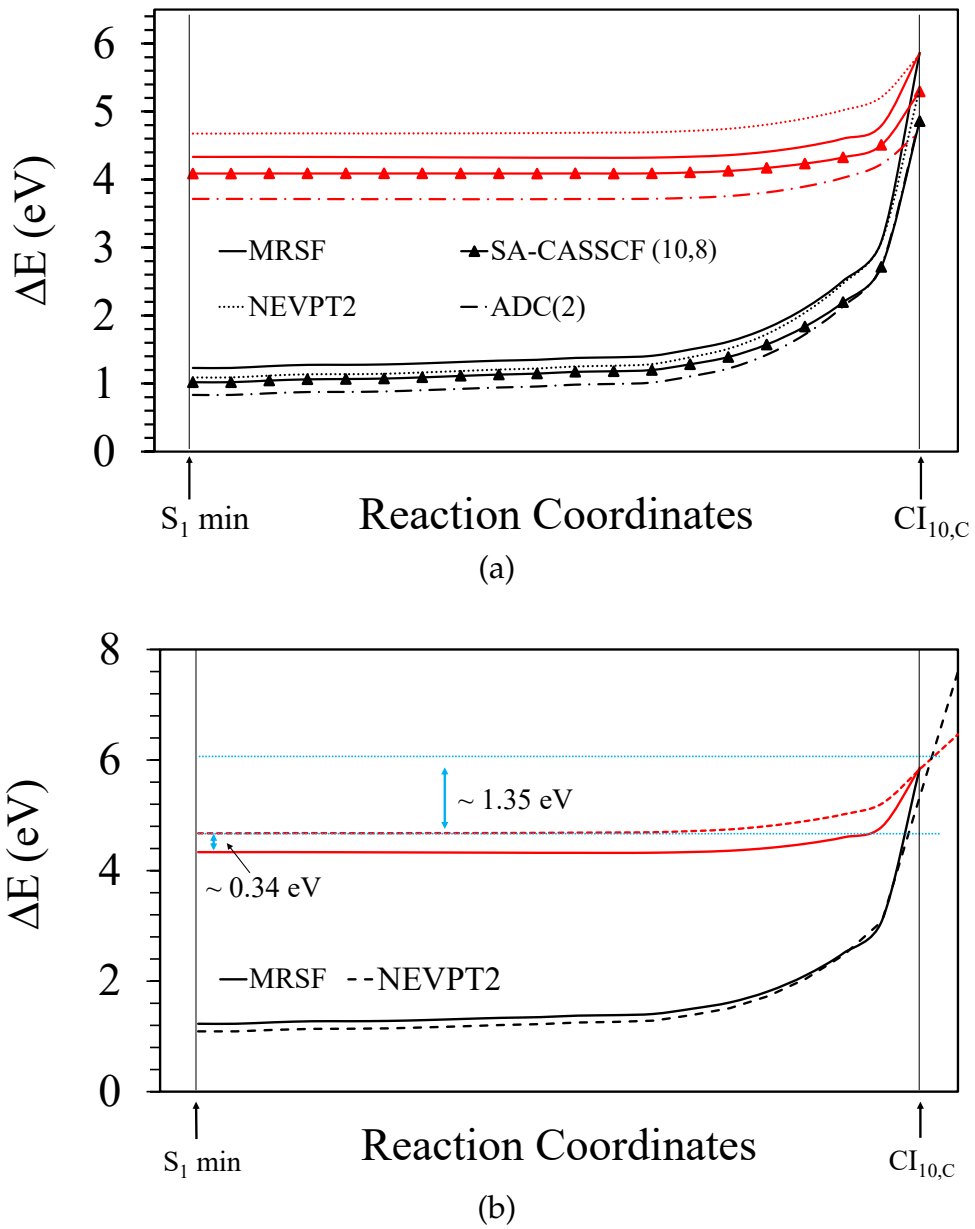

Figure S6: Upper panel: The S_1 (red) and S_0 (black) PES profiles along the S_1 MEP optimized with MRSF and connecting the $S_{1,min}$ and the $CI_{10,C}$ geometries. Lower panel: Comparison of the S_1 and S_0 energy profiles obtained by MRSF (solid lines) and NEVPT2 (dashed lines), where the NEVPT2 curves were extrapolated beyond the $CI_{10,C}$ geometry to reach crossing between the S_0 and S_1 curves.

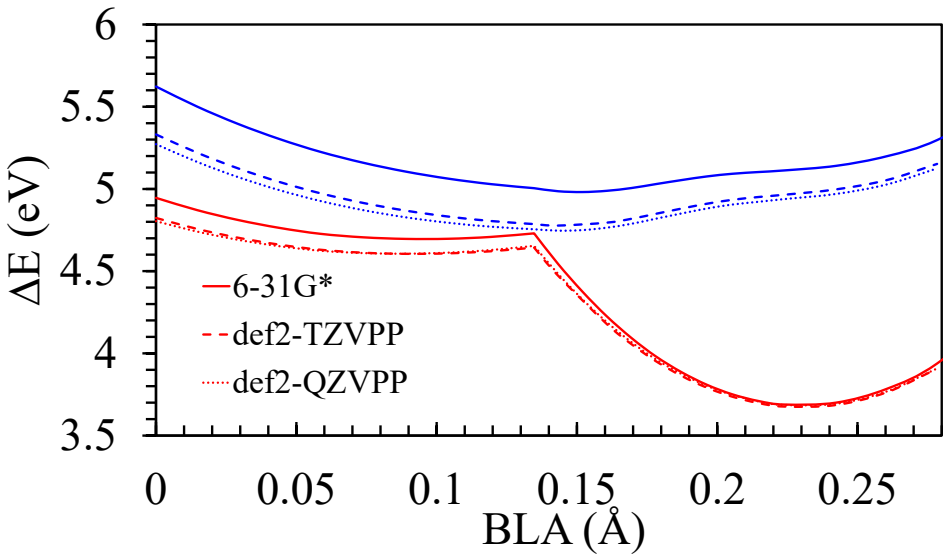

Figure S7: MEPs on the S_2 and S_1 PESs optimized using the NEB method with ADC(2) method and several basis sets. It connects the FC region, the $CI_{21,BLA}$, and the $S_{1,min}$ geometries. The geometries are taken from MRSF MEP results. It represents the S_2 (blue) and S_1 (red) PES profiles obtained with the 6-31G* (solid lines), def2-TZVPP (dashed line), and def2-QZVPP (dotted lines).

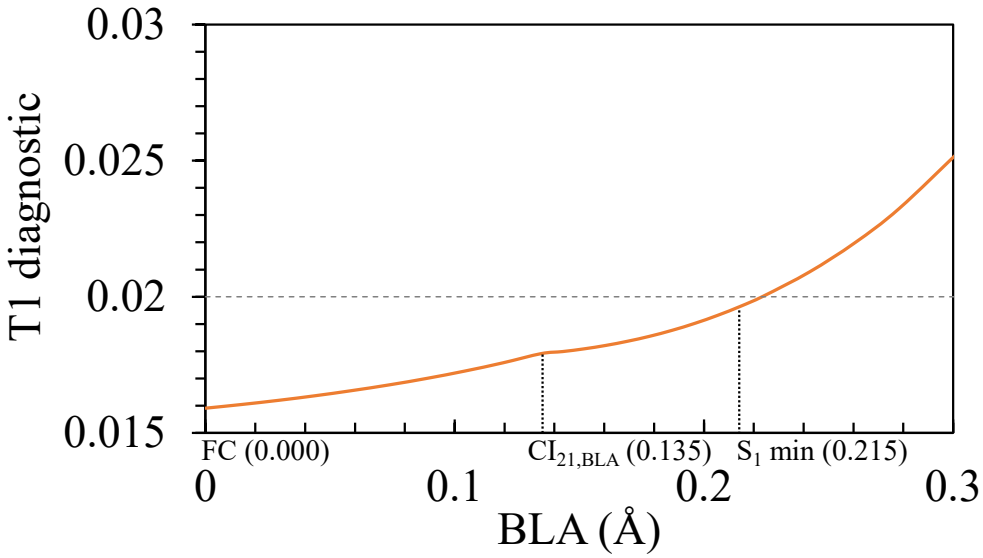

Figure S8: T1 diagnostic value of CCSD along the BLA MEPs. Gray horizontal dashed line shows the limiting value of 0.02 for the T1 diagnostic. The BLA values at FC, $CI_{21,BLA}$, and S_1 min are given in parentheses.

The nature of $CI_{21,BLA}$.

The $CI_{21,BLA}$ for S_2 to S_1 ultrafast transition is a symmetry-allowed seam, since both states belong to different irreducible representations of C_s, while the S_1/S_0 CIs are a same-symmetry seam. This particular seam structure along $\hat{g}$ and $\hat{h}$ branching plane vectors further increases the chances of nonadiabatic transition. It is noted that the abrupt change of state character at $CI_{21,BLA}$ turns the direction of BLA path (black circles) to its opposite, which can be due to the much steeper slope along the $n\pi^*$ surfaces at $CI_{21,BLA}$. This large difference in the slopes of the two diabatic surfaces would make the S_2 to S_1 transition unidirectional, producing a dramatic increase of S_1 population in Fig. 2 (a) and (b).

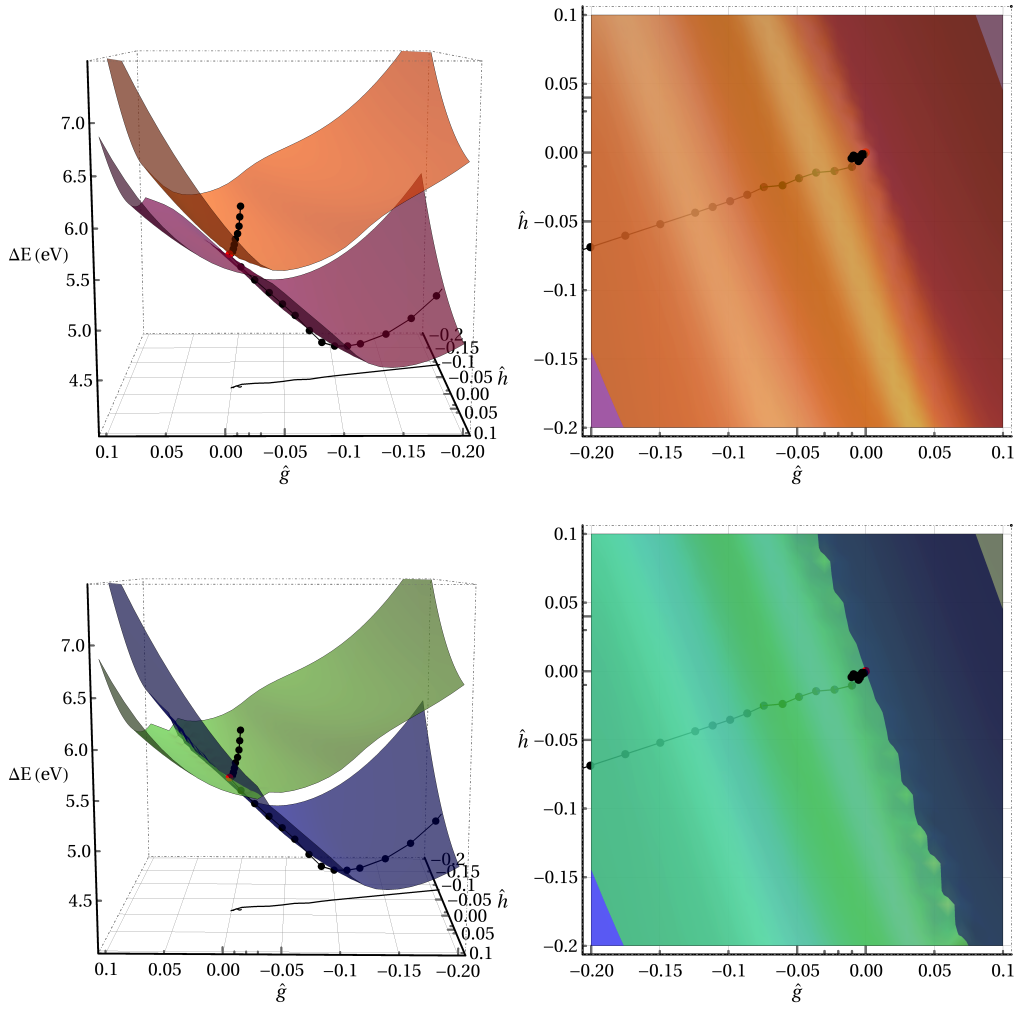

Figure S9: 3D Potential energy surface scans near the $CI_{21,BLA}$ using two normalized branching plane vectors (the gradient difference vector $\hat{g}$ and the derivative coupling vector $\hat{h}$) along with the BLA PES projected onto these two vectors. (a), (b) The orange and purple mesh represent S_2, S_1 PES respectively. (c), (d) The blue and green mesh represent $n\pi^*$, $\pi\pi^*$ PES respectively. The Black dots along with black thick line shows the BLA PES. Red dot represents the $CI_{21,BLA}$ point. In terms of the normalized $\hat{g}$ and $\hat{h}$ vectors, the displacements of the special poins on the plots are: FC (-0.01, -0.004), $CI_{21,BLA}$ (0.00, 0.00), and S_1 min (-0.11, -0.040).

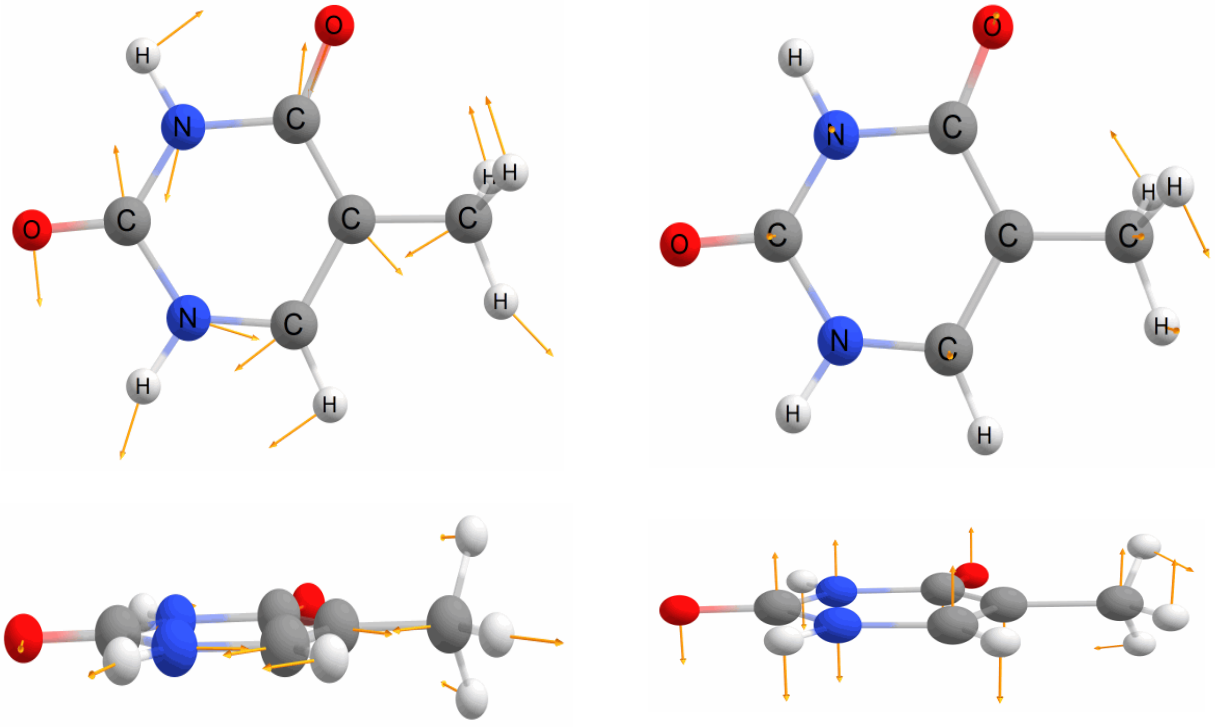

Figure S10: The gradient difference vector (g vector) and nonadiabatic coupling vector (h vector) at the $CI_{21,BLA}$. Upper panels and lower panels represents top view and side view respectively. The original g and h vectors were transformed in such a way that they represent in- and out-of-plan directions.[2]

Details of Nonadiabatic Molecular Dynamics (NAMD) Simulations

The three-state NAMD simulations were initiated by sampling the Wigner function of a canonical ensemble[26,27] at T = 300K around the S_0 equilibrium geometry. In this study, NAMD has been performed based on the fewest-switches surface-hopping algorithm,[28] and nonadiabatic coupling vectors are computed numerically by using a fast overlap calculation[29] using the locally modified GAMESS. Velocity Verlet is used for integration. The energy conservation during the hops were ensured by rescaling the velocities. Hundred trajectories were propagated using the NVE ensemble with a time-step size of 0.5 fs until 2000 fs for a propagation of the nuclear degrees of freedom and with a sub time-step size 10^{-5} fs for a propagation of the electronic degrees of freedom.[30] 11 trajectories failed due to SCF convergences. No corrections for decoherence was applied.

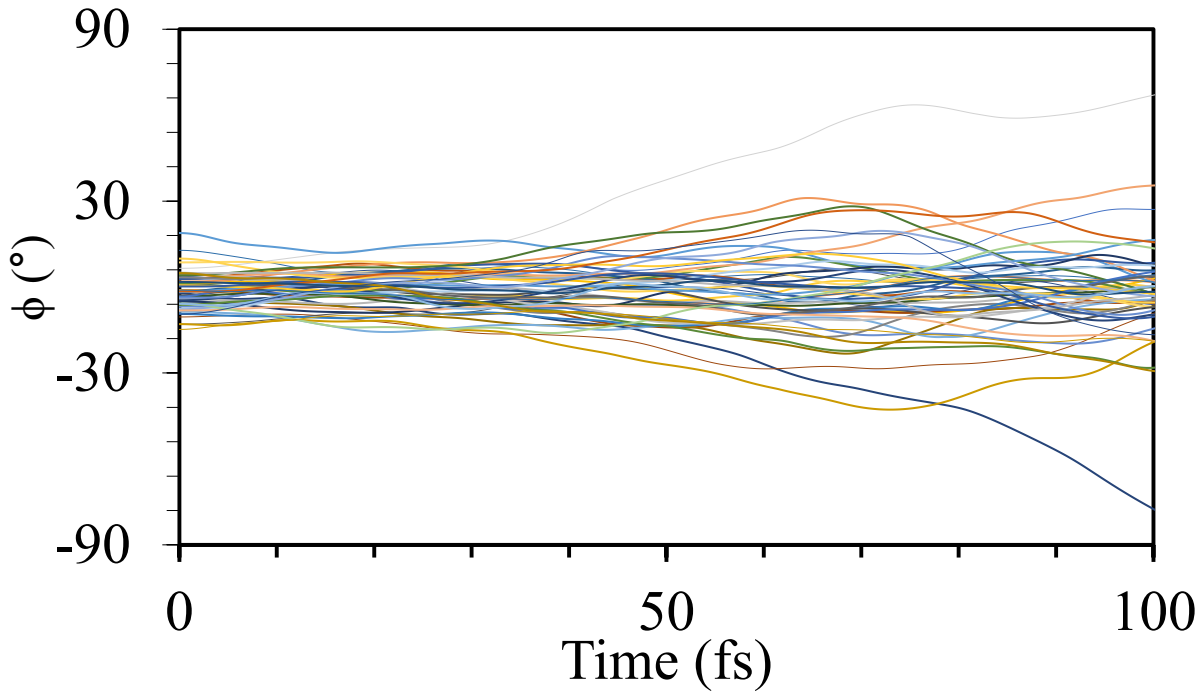

Figure S11: Time evolution of torsion (ϕ) along the simulation time until 100fs.

References

(1) Ozeki, K.; Sakabe, N.; Tanaka, J. The crystal structure of thymine. *Acta Crystallogr. B: Structural Crystallography and Crystal Chemistry* **1969**, *25*, 1038–1045.

(2) Zhu, X.; Yarkony, D. R. Non-adiabaticity: the importance of conical intersections. *Molecular Physics* **2016**, *114*, 1983–2013.

(3) Shao, Y.; Head-Gordon, M.; Krylov, A. I. The spin-flip approach within time-dependent density functional theory: Theory and applications to diradicals. *J. Chem. Phys.* **2003**, *118*, 4807–4818.

(4) Casanova, D.; Krylov, A. I. Spin-Flip Methods in Quantum Chemistry. *Phys. Chem. Chem. Phys.* **2020**, *22*, 4326–4342.

(5) Casida, M. E.; Jamorski, C.; Bohr, F.; Guan, J. G.; Salahub, D. R. In *NONLINEAR OPTICAL MATERIALS: THEORY AND MODELING*; Karna, S. P. and Yeates, A. T.,, Ed.; ACS SYMPOSIUM SERIES; 1996; Vol. 628; pp 145–163, Symposium on Nonlinear Optical Materials - Theory and Modeling, at the 208th National Meeting of the American-Chemical-Society, WASHINGTON, DC, AUG 21-25, 1994.

(6) Fiolhais, C.; Nogueira, F.; Marques, M. A. *A primer in density functional theory*; Springer Science & Business Media, 2003; Vol. 620.

(7) Casida, M. E.; Huix-Rotllant, M. Progress in time-dependent density-functional theory. *Annu. Rev. Phys. Chem.* **2012**, *63*, 287–323.

(8) Lee, S.; Shostak, S.; Filatov, M.; Choi, C. H. Conical Intersections in Organic Molecules: Benchmarking Mixed-Reference Spin–Flip Time-Dependent DFT (MRSF-TD-DFT) vs Spin–Flip TD-DFT. *J. Phys. Chem. A* **2019**, *123*, 6455.

(9) Lee, S.; Filatov, M.; Lee, S.; Choi, C. H. Eliminating spin-contamination of spin-flip time dependent density functional theory within linear response formalism by the

use of zeroth-order mixed-reference (MR) reduced density matrix. *J. Chem. Phys.* **2018**, *149*, 104101.

(10) Lee, S.; Kim, E. E.; Nakata, H.; Lee, S.; Choi, C. H. Efficient implementations of analytic energy gradient for mixed-reference spin-flip time-dependent density functional theory (MRSF-TDDFT). *J. Chem. Phys.* **2019**, *150*, 184111.

(11) McWeeny, R. *Methods of Molecular Quantum Mechanics*; Academic Press: London, 1992; pp 438–442.

(12) Tamm, I. Relativistic interaction of elementary particles. *J. Phys.(USSR)* **1945**, *9*, 449.

(13) Dancoff, S. Non-adiabatic meson theory of nuclear forces. *Phys. Rev* **1950**, *78*, 382.

(14) Horbatenko, Y.; Lee, S.; Filatov, M.; Choi, C. H. Performance Analysis and Optimization of Mixed-Reference Spin-Flip Time-Dependent Density Functional Theory (MRSF-TDDFT) for Vertical Excitation Energies and Singlet–Triplet Energy Gaps. *J. Phys. Chem. A* **2019**, *123*, 7991.

(15) Jónsson, H.; Mills, G.; Jacobsen, K. W. In *Classical and Quantum Dynamics in Condensed Phase Simulations*; Berne, B. J., Ciccotti, G., Coker, D. F., Eds.; World Scientific: Singapore, 1998; Chapter 16, pp 385–404.

(16) Kästner, J.; Carr, J. M.; Keal, T. W.; Thiel, W.; Wander, A.; Sherwood, P. DL-FIND: an open-source geometry optimizer for atomistic simulations. *J. Phys. Chem. A* **2009**, *113*, 11856–11865.

(17) Parker, S. M.; Roy, S.; Furche, F. Multistate hybrid time-dependent density functional theory with surface hopping accurately captures ultrafast thymine photodeactivation. *Phys. Chem. Chem. Phys.* **2019**, *21*, 18999–19010.

(18) Stojanović, L.; Bai, S.; Nagesh, J.; Izmaylov, A.; Crespo-Otero, R.; Lischka, H.; Barbatti, M. New Insights into the State Trapping of UV-Excited Thymine. *Molecules* **2016**, *21*, 1603.

(19) Asturiol, D.; Lasorne, B.; Worth, G. A.; Robb, M. A.; Blancafort, L. Exploring the sloped-to-peaked S 2/S 1 seam of intersection of thymine with electronic structure and direct quantum dynamics calculations. *Phys. Chem. Chem. Phys.* **2010**, *12*, 4949–4958.

(20) Zechmann, G.; Barbatti, M. Photophysics and deactivation pathways of thymine. *J. Phys. Chem. A* **2008**, *112*, 8273–8279.

(21) Fleig, T.; Knecht, S.; Hättig, C. Quantum-chemical investigation of the structures and electronic spectra of the nucleic acid bases at the coupled cluster CC2 level. *The Journal of Physical Chemistry A* **2007**, *111*, 5482–5491.

(22) Lorentzon, J.; Fuelscher, M. P.; Roos, B. O. Theoretical study of the electronic spectra of uracil and thymine. *Journal of the American Chemical Society* **1995**, *117*, 9265–9273.

(23) Abouaf, R.; Pommier, J.; Dunet, H. Electronic and vibrational excitation in gas phase thymine and 5-bromouracil by electron impact. *Chem. Phys. Lett.* **2003**, *381*, 486–494.

(24) Michaud, M.; Bazin, M.; Sanche, L. Measurement of inelastic cross sections for low-energy electron scattering from DNA bases. *Int. J. Radiat. Biol.* **2012**, *88*, 15–21.

(25) Chernyshova, I. V.; Kontros, E. J.; Markush, P. P.; Shpenik, O. B. Excitation of lowest electronic states of thymine by slow electrons. *Opt. Spectrosc.* **2013**, *115*, 645–650.

(26) Oppenheim, I.; Ross, J. Temperature Dependence of Distribution Functions in Quantum Statistical Mechanics. *Phys. Rev.* **1957**, *107*, 28–32.

(27) Davies, R. W.; Davies, K. T. R. On the Wigner Distribution Function for an Oscillator. *Ann. Phys.* **1975**, *89*, 261–273.

(28) Tully, J. C. Molecular dynamics with electronic transitions. *J. Chem. Phys.* **1990**, *93*, 1061.

(29) Lee, S.; Kim, E.; Lee, S.; Choi, C. H. Fast Overlap Evaluations for Nonadiabatic Molecular Dynamics Simulations: Applications to SF-TDDFT and TDDFT. *J. Chem. Theory Comput.* **2019**, *15*, 882.

(30) Mitrić, R.; Werner, U.; Bonačić-Koutecký, V. Nonadiabatic dynamics and simulation of time resolved photoelectron spectra within time-dependent density functional theory: Ultrafast photoswitching in benzylideneaniline. *J. Chem. Phys.* **2008**, *129*, 164118.